Improved Collaborative Non-Negative Matrix Factorization and Total Variation for Hyperspectral Unmixing

Yuan Yuan, *Senior Member, IEEE*, Zihan Zhang, and Qi Wang, *Senior Member, IEEE*

***Abstract*—Hyperspectral unmixing (HSU) is an important technique of remote sensing, which estimates the fractional abundances and the mixing matrix of endmembers in each mixed pixel from the hyperspectral image. Over the last years, the linear spectral unmixing problem has been approached as the sparse regression by different algorithms. Nevertheless, the huge solution space for individual pixels makes it difficult to search for the optimal solution in some HSU algorithms. Besides, the mixing relationship between adjacent pixels is not fully utilized as well. To better handle the huge solution space problem and explore the adjacent relationship, this article presents an improved collaborative non-negative matrix factorization and total variation algorithm (ICoNMF-TV) for HSU. The main contributions of this article are threefold: 1) a new framework named ICoNMF-TV based on non-negative matrix factorization method and TV regularization is developed to improve the performance of HSU algorithms; 2) unmixing efficiency is apparently improved; and 3) the robustness is enhanced. Experiment results on simulation dataset and real dataset demonstrate the proposed algorithm outperforms most of the similar sparse regression algorithms.**

***Index Terms*—Collaborative row sparsity, hyperspectral image unmixing, total variation.**

I. Introduction

HYPERSPECTRAL unmixing (HSU) is an important technique for remote sensing hyperspectral data exploitation. The task of HSU is to estimate the pure spectral signatures, called endmembers, and their corresponding fractions, called abundance, for each pixel of the hyperspectral image [1]. Thus, the spectral of pixels is resolved into a weighted combination of the endmembers. HSU is widely applied for other hyperspectral fields [2], [3].

Depending on the fundamental mixing models, the solutions of hyperspectral image unmixing can be separated into two types: nonlinear and linear models. Linear mixing models (LMM) assume that mixing occurs on a macroscopic scale and that the incident light only interacts with a single material. In LMM, when a pixel consists of more than one material, the observed spectral vector of the pixel will be a weighted sum of the endmembers representing the materials and noise coming from facilities. This article focuses on the HSU method with LMM. The main challenges for LMM are summarized as follows.

1) *Huge solution space:* The huge solution space is an important problem to solve for unmixing methods. To be specific, one mixed pixel consists of many endmembers with different abundance parameters. There are hundreds of possible combinations. In general, an image contains millions of pixels, so that the number of mixing combinations is almost uncountable without constraints.
2) *Mixing relationship between adjacent pixels:* The mixing relationship between adjacent pixels is relatively complex to describe, which is generally ignored by some common HSU methods. Many methods often focus on the mixed relationship of endmembers for individual pixel [4]. Nevertheless, the way how the endmembers are mixed between adjacent pixels has a great influence on the integrity of the abundance map [5]. Broadly speaking, a sophisticated unmixing method requires a concise explanation of the mixed connections between adjacent pixels.

According to the physical characteristics of abundance, we noticed that the abundance fraction matrix usually has zero-value rows. The fractional abundance of the same endmember has a correlation among neighboring pixels. This property gives us the method to reduce the solution space. In some kinds of sparse regression unmixing method, the abundance fraction matrix is often mapped into the whole large spectrum library as a subset to promote row sparsity. Since the speed and precision of sparse methods using libraries are not satisfactory, we kept the method without using the whole spectral libraries. Then, we built a right-sized and collaborative-row-sparse optimization variable matrix, which links with the abundance matrix, to complete the process of unmixing. In some image restoration problems, the correlation among neighboring pixels is often represented as the smooth transitions applying regularization methods. We transferred this method to describe our HSU problem with the total variation regularization.

After the above analysis, this article first proposed two constraints to reduce the solution space: the collaborative row sparsity constraint and total-variation regularization. With these constraints, this article developed a new hyperspectral image

Manuscript received May 23, 2019; revised August 23, 2019, December 14, 2019, and January 31, 2020; accepted February 23, 2020. Date of publication March 4, 2020; date of current version March 18, 2020. This work was supported by the National Natural Science Foundation of China under Grant 61632018, Grant 61825603, Grant U1864204, and Grant 61773316. *(Corresponding author: Qi Wang.)*

The authors are with the School of Computer Science and with the Center for Optical Imagery Analysis and Learning, Northwestern Polytechnical University, Xi'an 710072, China (e-mail: y.yuan1.ieee@qq.com; zihanzhang@mail.nwpu.edu.cn; crabwq@gmail.com).

Digital Object Identifier 10.1109/JSTARS.2020.2977399

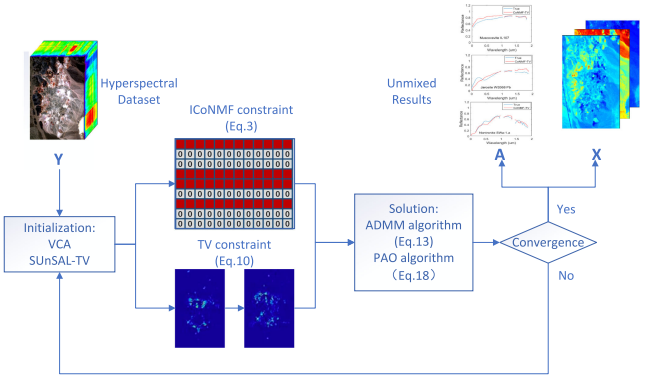

Fig. 1. ICoNMF-TV model. This figure shows the model proposed in this article, which is combined by collaborative row sparsity (CoNMF) constraint and total-variation regularization (TV) constraint.

unmixing framework termed improved collaborative non-negative matrix factorization and total variation algorithm (ICoNMF-TV), shown in Fig. 1. In this method, the robust non-negative matrix factorization (NMF) is applied to describe the row sparsity of the abundance coefficients. The solution space of the unmixing problem is sharply reduced to solve the huge solution space problem [6]. Then, the total variation regularization term is introduced to limit the smoothness between adjacent pixels. Adjacent pixels in hyperspectral images often contain the same substances with similar spectral characteristics [7]. The accuracy of unmixing can be effectively improved using this relationship in hyperspectral images. Further analysis shows that this kind of correlation is usually represented as the smoothness between neighboring pixels [8]. The main contributions are summarized as follows.

1) A new framework named ICoNMF-TV based on the NMF method and total variation (TV) regularization is developed to improve the performance of HSU algorithms. Different from the common combinations of TV term and sparse regression methods in existing algorithms, this article introduces the TV regularizer into the statistical methods. A novel optimization function for the NMF model is proposed to discuss. Experimental data indicate that the proposed algorithm is effective and yields good results.
2) Unmixing efficiency is apparently improved. Referring to [9], R-CoNMF uses sparse regression methods (SUnSAL [10] and CLSUnSAL [11]) to solve the objective function. Although it greatly shortens the unmixing time, the accuracy is still lower than some TV regularizers on top of sparse unmixing approaches such as CLSUnSAL-TV [8]. Based on the NMF model, ICoNMF-TV uses these TV regularizers for an abundance constraint. The experimental results show that the proposed method has a shorter unmixing time than the similar TV-based methods, and the accuracy exceeds the above algorithms. In summary, the algorithm proposed by this article improves the unmixing efficiency.
3) The robustness is enhanced. Unlike the sparse regression method, which is easily affected by the dataset condition and coefficient settings, the proposed method performs better on robustness. Meanwhile, it can be seen from the experiments that the proposed method is more stable than R-CoNMF under different signal noise ratio (SNR) settings and datasets.

The rest of this article is organized as follows. Section II reviews the related work. Section III elaborates the proposed algorithm. Sections IV and V compares the performances of six different HSU method on simulation dataset and real dataset. Finally, we give a conclusion of this article and present our further work in Section VI.

II. Related Work

In recent years, numerous unmixing methods have been introduced using LMM. Referring to the elaboration of J. Bioucas-Dias, these methods fall into four categories [12].

A. Geometrical Methods

Each pixel in the HSI can be viewed as a vector in a multidimensional space, and each band corresponds to an axis in the space. Thus, HSU has been transformed into a common geometrical problem [13]. These methods apply some basic geometric facts to solve HSU, which can be further categorized as minimum volume methods [14]. Appropriate examples of methods applying these two kinds are vertex component analysis (VCA) [15], and minimum volume simplex analysis [16]. Since it only makes use of the original spectral information, geometrical method is fully automatic and speedy to some extent. Nonetheless, as a traditional method, it tends to be influenced by abnormal pixels, and the precision of it still needs to be improved.

B. Statistical Methods

Hyperspectral images can be regarded as huge data cubes. Then, HSU is formulated as a statistical inference problem. In this way, the LMM model is redefined as the combination of applicable math assumptions [17]. Resorted to the statistic framework, unmixing can be realized by different update steps. Dirichlet components mixture uses Dirichlet densities as the prior abundance fraction basing on Lagrange optimization. Similarly, joint Bayesian endmember extraction and linear unmixing [18] use posterior distribution in the hierarchical Bayesian model. NMF is an important part of this kind of method [6], [19], which is an unmixing method based on statistical matrix factorization, such as CoNMF [20], ℓ_1-NMF [21], $\ell_{1/2}$-NMF [22], and R-CoNMF [9]. The remarkable effect of these algorithms is that the running speed is usually fast [23]. As another large category of the traditional unmixing methods, it still acquires the number of endmembers formerly, and the precision of it is usually not very satisfactory.

C. Sparse Regression Methods

Under the assumption that the observed spectra can be represented as linear combinations of spectral signatures, the sparse regression method is widely used [24], [25]. These methods mostly use some known spectral libraries as the endmembers collections [26], [27], such as SUnSAL [10], SUnSAL-TV [7],

CLSUnSAL [11], and CLSUnSAL-TV [8]. These algorithms can get high-precision results but run slower.

D. Deep Learning Methods

Data-driven neural networks are also used for abundance estimation [28]. By setting custom layers and weight constraints, several pre-existing neutral networks can be trained to unmix mixed pixels, such as autoencoder network [29], differential search neural network [30]. Mature neural networks can unmix a hyperspectral image pixel by pixel with an appropriate precision. Nonetheless, the speed of deep learning methods is remained to be discussed since the time cost by training networks is usually long and the number of pixels in HSI is often large [31], [32]. These methods still lack sufficient real training datasets.

The aforementioned four kinds of methods all can be applied to HSU, but the accuracy and speed may be improved if some methods are selectively combined. In order to unmix pixels in HSIs totally, a relatively superior solution for the objective function of each algorithm in LMM is necessary. However, research about getting relatively superior solutions in unmixing is challenging and most of them still cannot balance the running speed and the accuracy of results so far. The NMF method provides a way to process matrix data in batches, which makes it possible to achieve a good solution quickly. NMF-based methods can be roughly divided into two categories: structure extensions and sparse regression constraints. To reduce the solution space, extension algorithms based on the NMF method have been proposed with modified structures, including semi-NMF [33], symmetric NMF [34], nonsmooth NMF [35], and multilayer NMF [36]. Researchers have also tried to impose further sparse regression constraints to improve NMF-based methods, in ℓ_1-NMF [21], $\ell_{1/2}$-NMF [22], and R-CoNMF [9]. Besides, most studies about unmixing in LMM are limited to individual pixel studies and need to be explored into the adjacent pixels. The SUnSAL-TV method proposed by Iordache *et al.* gives an illuminating description for the mixing relationship of adjacent pixels with a total variation regularization term. Inspired by these methods, this article attempts to propose a new algorithm to solve the above problems and take into account the accuracy and speed simultaneously.

The linear mixture model (LMM) assumes that each pixel spectrum in any given spectral band can be linearly combined by the endmember spectrums [12], which means for each pixel, the LMM can be mathematically expressed as

$$y_j = \sum_{i=1}^{q} m_{ij} s_i + n_j \tag{1}$$

where y_j is the measured value of the reflectivity for a mixed pixel on the spectral band j; m_{ij} is the reflectivity of the endmember i on the band j; s_i is the abundance values of endmember i in this mixed pixel; n_j is the process noise, and q is the number of endmembers.

According to the form of NMF mentioned above [6], (1) can be presented as

$$\begin{aligned} &\mathbf{Y} = \mathbf{MS} + \mathbf{N} \\ &\text{s.t.} \quad \mathbf{S} \geq 0, \mathbf{1}_P^T \mathbf{S} = \mathbf{1}_n^T \end{aligned} \tag{2}$$

where $\mathbf{Y} \equiv [y_1, \ldots, y_n] \in \mathbb{R}^{d \times n}$ is the hyperspectral image matrix with n pixels and d spectral bands; $\mathbf{M} \equiv [m_1, \ldots, m_q] \in \mathbb{R}^{d \times q}$ is the mixing matrix with q endmembers; m_i is the ith endmember signature; $\mathbf{S} \equiv [s_1, \ldots, s_n] \in \mathbb{R}^{q \times n}$ is the abundance matrix; s_i denotes the endmember fractions, for pixels $i = 1, \ldots, n$; $\mathbf{S} \geq 0$ is the non-negative abundance constraint for the component-wise method; $\mathbf{1}_P^T \mathbf{S} = \mathbf{1}_n^T$ is the abundance sum to one constraint for the physics characteristic of abundance vector; $\mathbf{N}$ is the noise from facilities and the measure process. This section introduced the NMF equation in LMM, which is the basic function of our algorithm. Then, we will discuss the collaborative sparsity constraint further basing on it.

III. Methodology

A. Improved Collaborative Sparsity Constraint Term

According to the physical characteristics of abundance, we noticed that the abundance fraction matrix usually has zero-value rows. This property gives us the method to reduce the solution space. Considering some kinds of sparse regression unmixing method, the abundance fraction matrix is often mapped into the whole large spectrum library as a subset to promote row sparsity. Since the speed and precision of sparse methods using libraries are not satisfactory, we keep the method without using the libraries. Then, a collaborative-row-sparse optimization variable matrix is built, which links with the abundance matrix, to complete the process of unmixing. The global collaborative sparsity constraint can be implemented by promoting the row-sparsity of an abundance matrix [20].

Let $\mathbf{A} \equiv [a_1, \ldots, a_q] \in \mathbb{R}^{d \times q}$ and $\mathbf{X} \in \mathbb{R}^{q \times n}$ be optimization variable matrixes, which links with the practical mixing matrix $\mathbf{M}$ and the abundance matrix $\mathbf{S}$; q is a number given. Then, we use the collaborative-row-sparse optimization term in

$$\min_{\mathbf{x}} \|\mathbf{X}\|_{2,1} \tag{3}$$

where $\|\mathbf{X}\|_{2,1} \equiv \sum_{i=1}^{q} \|\mathbf{x}^i\|_2$ is the $\ell_{2,1}$ mixed norm of $\mathbf{X}$.

Let Λ denote the row number of the abundance matrix, we assume

$$\mathbf{A}_{|\Lambda} \equiv [a_i, i \in \Lambda] \tag{4}$$

$$\mathbf{X}^{|\Lambda} \equiv [(x^i)^T, i \in \Lambda]^T \tag{5}$$

moreover, let

$$\text{rowsupp}(\mathbf{X}) \equiv \{i, \mathbf{x}^i \neq \mathbf{0}\} \tag{6}$$

with above assumptions, we introduce

$$\widehat{\mathbf{M}} \equiv \widehat{\mathbf{A}}_{|\text{rowsupp}(\widehat{\mathbf{X}})} \tag{7}$$

$$\widehat{\mathbf{S}} \equiv \widehat{\mathbf{X}}^{|\text{rowsupp}(\widehat{\mathbf{X}})} \tag{8}$$

where $\widehat{\mathbf{M}} \simeq \mathbf{M}$ and $\widehat{\mathbf{S}} \simeq \mathbf{S}$; Λ is the row number of abundance matrix; this model is shown in Fig. 1.

Thus, the volume terms and data fidelity propel the optimization matrixes $(\mathbf{A}, \mathbf{X})$ to unmixing solutions extremely close to the practical matrixes $(\mathbf{M}, \mathbf{S})$. $(\mathbf{A}, \mathbf{X})$ can be accurately calculated as a common sparsity regression problem. We will

apply the effective constraint term described in this section to NMF objective function in the next part.

B. Optimization Function of ICoNMF

Based on the above assumptions, we undertake the estimation of $\mathbf{M}$ and $\mathbf{S}$ by searching a robust solution for this ICoNMF optimization function [9], as in

$$\min_{\mathbf{A},\mathbf{X}} \left(\frac{1}{2}\right) \|\mathbf{Y}-\mathbf{A}\mathbf{X}\|_F^2 + \alpha\|\mathbf{X}\|_{2,1} + \frac{\beta}{2}\|\mathbf{A}-\mathbf{P}\|_F^2$$
$$\text{s.t.} \quad \mathbf{X}\in\mathcal{S}_{q-1}, \mathbf{A}\in\mathcal{A}_{q-1} \tag{9}$$

where $\|\cdot\|_2$ is the Euclidean norm; $\|\cdot\|_F$ is the Frobenius norm; $\mathbf{A}\equiv[a_1,\ldots,a_q]\in\mathbb{R}^{d\times q}$ and $\mathbf{X}\in\mathbb{R}^{q\times n}$; $\|\mathbf{X}\|_{2,1}\equiv\sum_{i=1}^{q}\|\mathbf{x}^i\|_2$ denotes the collaborative-row-sparse optimization term explained in the last section; $\mathbf{P}\equiv[y_{i1},\ldots,y_{iq}]$ is a collection of q observed spectrum vectors deduced by the pure-pixel algorithm, that is, it is very close to the extreme simplex; α and β are empirical regularization parameters we set; $\mathcal{S}_{q-1}$ is a set of $q\times n$ matrices the columns of which belong to the probability simplex with dimension $q-1$; and $\mathcal{A}_{q-1}$ is a set of $d\times q$ matrices, the columns of which belong to an affine set. The dimension of this set is $q-1$. This dimension describes $\mathbf{Y}$ best according to the mean square error. This optimization function avoids the inferiority of violating the sum-to-one constraint, which usually occurs in real datasets.

In detail, the optimization function shown in (9) has three terms: the data fidelity term $\|\mathbf{Y}-\mathbf{A}\mathbf{X}\|_F^2$, which guarantees solutions of unmixing with low reconstruction error; the $l_{2,1}$ mixed norm $\|\mathbf{X}\|_{2,1}$, which guarantees the row-sparsity of $\mathbf{X}$, that is, it guarantees solution matrices with setting whole rows $\mathbf{x}^i$ to zero; and the term $\|\mathbf{A}-\mathbf{P}\|_F^2$, which pushes columns of $\mathbf{A}$ to the given pure-pixel-based solution $\mathbf{P}$. This article uses VCA algorithm as pure-pixel algorithm to estimate $\mathbf{P}$, which is used by most unmixing methods to obtain the initial value.

C. Total Variation Regularity Term

According to the physical characteristics of abundance, we noticed that the fractional abundance of the same endmember correlates neighboring pixels. This property gives us the method to reduce the solution space. This kind of correlation among neighboring pixels is often represented as the smoothness using regularization methods. We transferred this method to describe our HSU problem with the total variation regularization [7], as in

$$\min_{\mathbf{X}} TV(\mathbf{X}) \tag{10}$$

where

$$TV(\mathbf{X}) = \|\mathbf{H}_h\mathbf{X}\|_1 + \|\mathbf{H}_v\mathbf{X}\|_1 \tag{11}$$

with

$$\begin{cases} \mathbf{H}_h\mathbf{X} = x_{i,j} - x_{i-1,j} \\ \mathbf{H}_v\mathbf{X} = x_{i,j} - x_{i,j-1}. \end{cases} \tag{12}$$

TV portrays the smoothness constraint for the abundance fraction of the same endmember among adjacent pixels; i is the collection of horizontal position and j is the vertical adjacent pixels in the HSI; according to the alternating direction method of multipliers [8], $\mathbf{H}_h:\mathbb{R}^{m\times n}\to\mathbb{R}^{m\times n}$ describes a linear operator calculating the horizontal differences between the pixels in $\mathbf{X}$ and its adjacent pixels; $\mathbf{H}_v:\mathbb{R}^{m\times n}\to\mathbb{R}^{m\times n}$ describes a linear operator calculating the vertical differences between the pixels in $\mathbf{X}$ and its adjacent pixels.

D. ICoNMF-TV Model

After providing the above definitions, we can now implement the sparse unmixing by seeking a solution for the following NMF optimization problem, as in

$$\min_{\mathbf{A},\mathbf{X}}\left(\frac{1}{2}\right)\|\mathbf{Y}-\mathbf{A}\mathbf{X}\|_F^2+\alpha\|\mathbf{X}\|_{2,1}+\frac{\beta}{2}\|\mathbf{A}-\mathbf{P}\|_F^2+\lambda_{\text{TV}}TV(\mathbf{X})$$
$$\text{s.t. } \mathbf{X}\in\mathcal{S}_{q-1}, \mathbf{A}\in\mathcal{A}_{q-1} \tag{13}$$

where $\|\mathbf{X}\|_{2,1}\equiv\sum_{i=1}^{q}\|\mathbf{x}^i\|_2$ and ICoNMF optimization function (9) are mentioned in Sections III-A and III-B; $\text{TV}(\mathbf{X})\equiv\sum_{\{i,j\}\in\varepsilon}\|x_i-x_j\|_1$ is mentioned in Section III-C; $\lambda_{\text{TV}}\geq 0$ is regularization parameters.

With these definitions in the above sections, we rewrite the optimization (13) as in

$$\min_{\mathbf{A}\in\mathbb{R}^{d\times q},\mathbf{X}\in\mathbb{R}^{q\times n}} L(\mathbf{A},\mathbf{X}) \tag{14}$$

where

$$L(\mathbf{A},\mathbf{X}) \equiv \left(\frac{1}{2}\right)\|\mathbf{Y}-\mathbf{A}\mathbf{X}\|_F^2+\alpha\|\mathbf{X}\|_{2,1}+\frac{\beta}{2}\|\mathbf{A}-\mathbf{P}\|_F^2 + \lambda_{\text{TV}}\|\mathbf{H}\mathbf{X}\|_{1,1}+\ell_{\mathcal{S}_{q-1}}(\mathbf{X})+\ell_{\mathcal{A}_{q-1}}(\mathbf{A}) \tag{15}$$

where $\ell_{\mathcal{S}_{q-1}}:\mathbb{R}^{q\times n}\to\mathbb{R}\cup\{+\infty\}$ and $\ell_{\mathcal{A}_{q-1}}:\mathbb{R}^{d\times q}\to\mathbb{R}\cup\{+\infty\}$ describe the indicator function of collections $\mathcal{S}_{q-1}$ and $\mathcal{A}_{q-1}$; i.e.,

$$\ell_{\mathcal{S}_{q-1}}(\mathbf{X}) = \begin{cases} +\infty & \mathbf{X}\notin\mathcal{S}_{q-1} \\ 0 & \text{otherwise} \end{cases} \tag{16}$$

and

$$\ell_{\mathcal{A}_{q-1}}(\mathbf{A}) = \begin{cases} +\infty & \mathbf{A}\notin\mathcal{A}_{q-1} \\ 0 & \text{otherwise.} \end{cases} \tag{17}$$

E. Solution for ICoNMF-TV Model

Since the F-norm function is convex and the feasible region is nonconvex, the data fidelity term $\frac{1}{2}\|\mathbf{Y}-\mathbf{A}\mathbf{X}\|_F^2$ in (14) is a nonconvex optimization. Thus, we apply the proximal alternating optimization (PAO) [37], which can converge to the critical point of nonconvex optimization functions under some conditions. Provided $(\mathbf{A}_{(0)},\mathbf{X}_{(0)})$ by VCA, PAO build the solution sequence [9]

$$(\mathbf{A}_t,\mathbf{X}_t)\to(\mathbf{A}_{t+1},\mathbf{X}_t)\to(\mathbf{A}_{t+1},\mathbf{X}_{t+1}) \tag{18}$$

where

$$\mathbf{A}_{t+1} = \arg\min_{\mathbf{A}} L(\mathbf{A},\mathbf{X}_{(\mathbf{t})}) + \frac{\lambda_t}{2}\|\mathbf{A}-\mathbf{A}_{(t)}\|_F^2 \tag{19}$$

$$\mathbf{X}_{t+1} = \arg\min_{\mathbf{X}} L(\mathbf{A}_{t+1},\mathbf{X}) + \frac{\mu_t}{2}\|\mathbf{X}-\mathbf{X}_{(t)}\|_F^2 \tag{20}$$

where λ_t, μ_t, for $t = 0, 1, \ldots$, are sets of positive numbers. We notice that the above sequences can be represented as the 2-block nonlinear Gauss–Seidel solution in the regularized view.

Based on this Gauss–Seidel solution, we introduce

$$(\mathcal{A}_{q-1} \equiv \{\mathbf{z} \in \mathbb{R}^d : \mathbf{z} = \overline{\mathbf{y}} + \mathbf{V}\boldsymbol{\alpha}, \boldsymbol{\alpha} \in \mathbb{R}^{q-1}\} \tag{21}$$

where $\bar{\mathbf{y}}$ is the sample average observation vector; $\mathbf{V} \in \mathbf{R}^{d\times(q-1)}$ is a matrix consisting of the first $(q-1)$ principal components of $\mathbf{Y}$; the columns of $\mathbf{V}$ are orthogonal, that is, $\mathbf{V}^T\mathbf{V} = \mathbf{I}_{q-1}$, where $\mathbf{I}_{q-1}$ is the identity matrix with $(q-1)$ dimension.

Define $\overline{\mathbf{Y}} \equiv [\overline{y}_1, \ldots, \overline{y}_{q-1}]$, (21) can be represented as in

$$\mathbf{A} = \overline{\mathbf{Y}} + \mathbf{V}\boldsymbol{\Delta} \tag{22}$$

then, we can conclude that any $\mathbf{A} \in \mathcal{A}_{q-1}$ holds a unique representation of the form (22), with

$$\boldsymbol{\Delta} = \mathbf{V}^T(\mathbf{A} - \overline{\mathbf{Y}}). \tag{23}$$

The procedure (18)–(20) can be interpreted as a regularized version of the two-block nonlinear Gauss–Seidel method [38]. Formula (22)–(24) is an instance of the class considered in [37], where optimization (24) is considered as a small size quadratic problem. According to [37], formula (25) is obtained by applying formula (22)–(24) into (19). Thus, the solution to the optimization (19) is

$$\mathbf{A}_{(t+1)} = \overline{\mathbf{Y}} + \mathbf{V}\boldsymbol{\Delta}_{(t+1)} \tag{24}$$

where

$$\begin{aligned}\boldsymbol{\Delta}_{(t+1)} = \mathbf{V}^T((\mathbf{Y} - \overline{\mathbf{Y}})\mathbf{X}_{(t)}^T + \beta(\mathbf{P} - \overline{\mathbf{Y}}) + \lambda_t\boldsymbol{\Delta}_{(t)}) \\ \cdot (\mathbf{X}_{(t)}\mathbf{X}_{(t)}^T + (\beta + \lambda_t)\mathbf{I})^{-1}\end{aligned} \tag{25}$$

where $\mathbf{I}$ is an identity matrix with suitable size; $(\cdot)^T$ is the transpose operator.

Provided $\mathbf{Y}'_{(t)} \equiv [\mathbf{Y}^T\sqrt{\mu_t}\mathbf{X}_{(t)}^T]^T$ and $\mathbf{A}'_{(t+1)} \equiv [\mathbf{A}_{(t+1)}^T \sqrt{\mu_t}\mathbf{I}]^T$, the optimization (20) is rewritten as

$$\begin{aligned}\min_{\mathbf{X}} \frac{1}{2}\|\mathbf{Y}'_t - \mathbf{A}_{(t+1)}\mathbf{X}\|_F^2 + \alpha\|\mathbf{X}\|_{2,1} \\ + \lambda_{TV}\|\mathbf{H}\mathbf{X}\|_{1,1} + \ell_{\mathcal{S}_{q-1}}(\mathbf{X})\end{aligned} \tag{26}$$

which is opportunely the constrained $\ell_2 - \ell_{2,1}$ and TV optimization computed by CLSUnSAL-TV [8], which is the generation of sparse regression unmixing by SUnSAL-TV [7] algorithm.

Now, we have completed the solution of our model. The pseudocode for the ICoNMF-TV algorithm is shown in Algorithm 1. The implementation process of the ICoNMF-TV framework proposed in this article can be decomposed into two parts: in the calculation of mixing matrix part, the computational complexity is dominated by calculations of $\mathbf{A}_{(t+1)}$ in lines 13 and 14, which is in NMF method. The core term in the calculations are $\mathbf{Y}\mathbf{X}_{(t)}^T$ and $\mathbf{X}_{(t)}\mathbf{X}_{(t)}^T$, from which the computation complexity of $\mathbf{A}_{(t+1)}$ is $\mathcal{O}(2q^2n)$; in the calculation of abundance matrix part, the computational complexity is dominated by calculations of $\mathbf{X}_{t+1}$, which is in CLSUnSAL-TV method. The computation complexity of CLSUnSAL-TV is $\mathcal{O}(Nnq \cdot \max(q, \log n))$, where N is the iterations number [8]. It should be noticed that q is higher than $\log n$ in our algorithm. Thus, the computation complexity of this part is $\mathcal{O}(Nnq^2)$. Therefore, we can get the conclusion that ICoNMF-TV complexity per iteration is controlled by the $\mathbf{X}_{(t+1)}$ term and is approximately given by $\mathcal{O}(Nnq^2)$.

Algorithm 1: Improved Collaborative Nonnegative Matrix Factorization and Total Variation (ICoNMF-TV).

Input: Hyperspectral image matrix $\mathbf{Y}$; Iterations N; Regularity parameters α, β, λ_t, μ_t; Number of the endmembers q; Stopping threshold δ; A quite small number θ

1: $\mathbf{U} \in \mathbb{R}^{d\times q} \leftarrow$ HySime$(\mathbf{Y}, q)$ //orthogonal basis
2: $\mathbf{Y} \leftarrow \mathbf{U}^T\mathbf{Y}; \bar{\mathbf{Y}} \leftarrow \bar{y}\mathbf{1}_q^T$
3: $\bar{\mathbf{V}} = orth(\mathbf{Y} * \mathbf{Y}^T/n - yy^T, q-1)$
4: $\mathbf{A}_{(0)} \leftarrow VCA(\mathbf{Y}, q)$
5: $\triangle_{(0)} = \mathbf{V}^T(\mathbf{A}_{(0)} - \mathbf{Y})$
6: $\mathbf{P} \leftarrow \mathbf{A}_{(0)}$
7: $\mathbf{X}_{(0)} \leftarrow SUnSAL - TV(\mathbf{A}_{(0)}, \mathbf{Y})$
8: $\epsilon_0 = \infty; t = -1$
9: **repeat**
10: $t \leftarrow t + 1$ //optimize with respect to $\mathbf{A}$
11: $update\ \boldsymbol{\Delta}_{(t+1)}\ using\ Eq.(25)$
12: $update\ \mathbf{A}_{(t+1)}\ using\ Eq.(24)$
13: $\mathbf{Y}'_{(t)} \leftarrow [\mathbf{Y}^T\sqrt{\mu_t}\mathbf{X}_{(t)}^T]^T$
14: $\mathbf{A}'_{(t+1)} \leftarrow [\mathbf{A}_{(t+1)}^T\sqrt{\mu_t}\mathbf{I}]^T$
15: $\mathbf{X}_{(t+1)} \leftarrow$CLSUnSAL-TV$(\mathbf{A}_{(t+2)}, \mathbf{Y}'_{(t)}, \alpha)$
16: $\epsilon_{(t)} \leftarrow \| \mathbf{Y} - \mathbf{A}_{(t)}\mathbf{X}_{(t)} \|$
17: **until** $\| \epsilon_t - \epsilon_{(t-1)} \| / \| \mathbf{F} \|_F > \delta$ and $t \le N$
18: $\Lambda = \emptyset$
19: **for** $i = 1$ **to** q **do**
20: **if** $\| \mathbf{x}_{(t)}^i \| \le \theta$ **then**
21: $\Lambda \leftarrow \Lambda \cup \{i\}$
22: **end if**
23: **end for**
24: $\hat{\mathbf{A}} \leftarrow \mathbf{U}\mathbf{A}_{(t)|\Lambda}; \hat{\mathbf{X}} \leftarrow \mathbf{X}_{(t)|\Lambda}$

Output: Estimated spectral signatures $\hat{\mathbf{A}}$ and abundance fractions $\hat{\mathbf{X}}$

IV. Experiments With Simulated Data

In this section, we illustrate the unmixing performance achieved by including the TV regularizer on top of the collaborative non-negative matrix method for spectral unmixing using the simulated hyperspectral dataset.

The goal is to analyze the influence of the TV regularizer and CoNMF term in the unmixing results. This section is organized as follows. Section IV-A describes how the simulated dataset is generated. Since the noiseless case is trivial, we only consider scenes affected by noise. Section IV-B describes the considered performance discriminators. Section IV-C concludes with a summary of the most relevant aspects observed in our simulated data experiments.

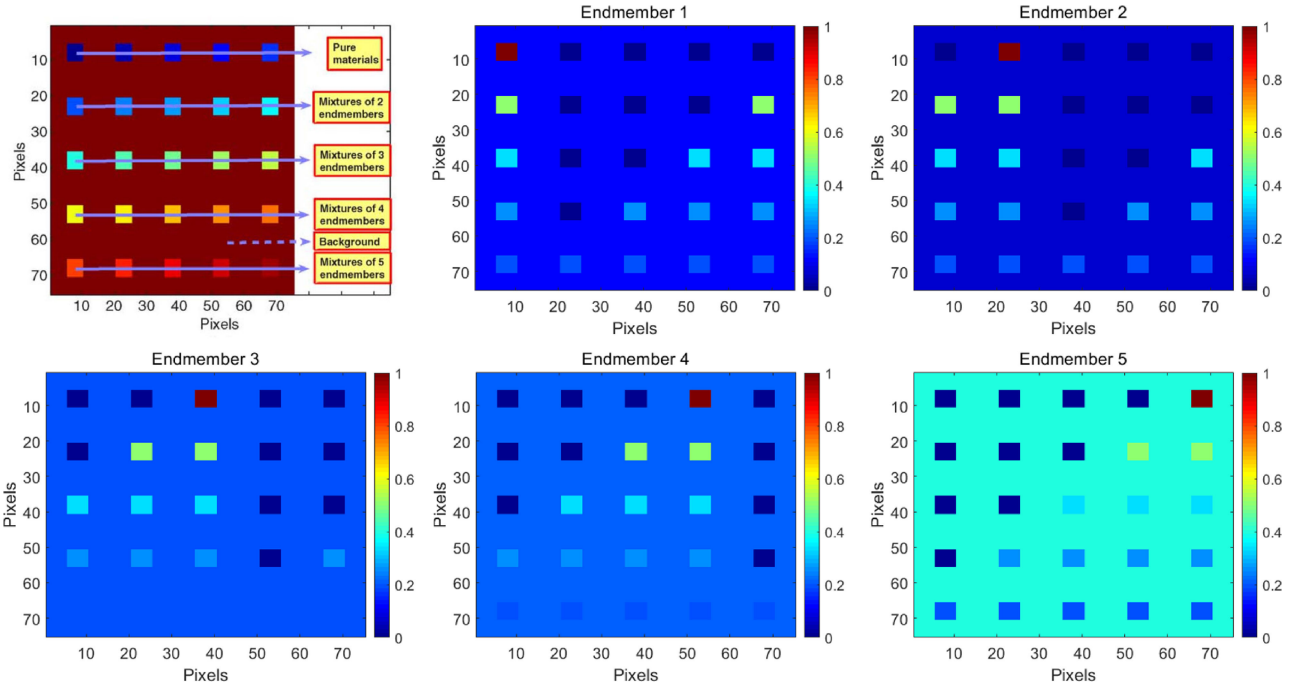

Fig. 2. Simulated image and five true fractional abundances of endmembers in the simulated dataset.

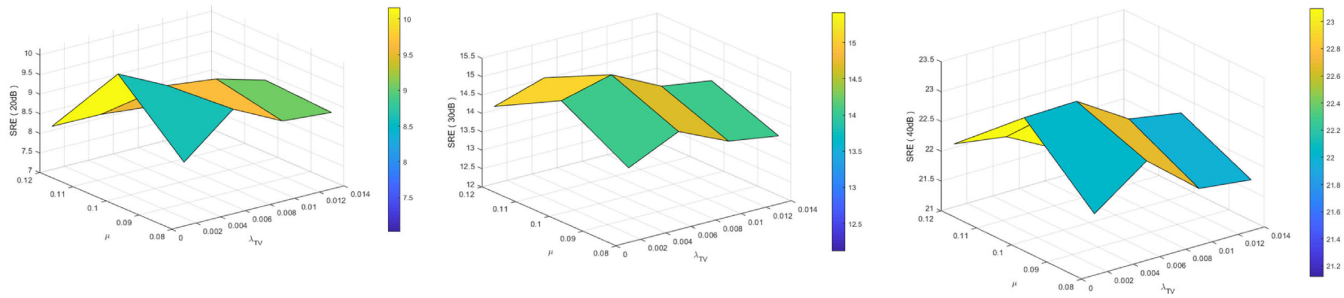

Fig. 3. SRE(dB) with different parameters μ and λ_{TV} obtained by ICoNMF-TV in different noise levels.

A. Simulated Dataset

The spectral library used in our simulated experiment is $\mathbf{A} \in \mathbb{R}^{224\times240}$. This spectral library is made by selecting 240 materials randomly in the USGS spectral library, which was open to the public in 2007. The spectrum interval is $0.4-2.5\ \mu$m, the spectral signatures of which is provided in 224 spectral bands. Select five spectral signatures as the endmembers to generate linearly a simulation dataset. This simulation dataset has pixels and each pixel has spectral bands. Fig. 4 shows the spectral characteristic curves of these five endmembers. Fig. 2 represents the simulated image and the real abundance images of the five endmembers. There are both pure pixels and mixed pixels consist of 2–5 endmembers in the simulated data. These pixels are evenly distributed in the fixed square area. The background pixels of the simulated data consist of five identical endmember mixtures, and their respective abundance coefficients are fixed at 0.1149, 0.0742, 0.2003, 0.2055, and 0.4051. At the same time, to test the antinoise performance

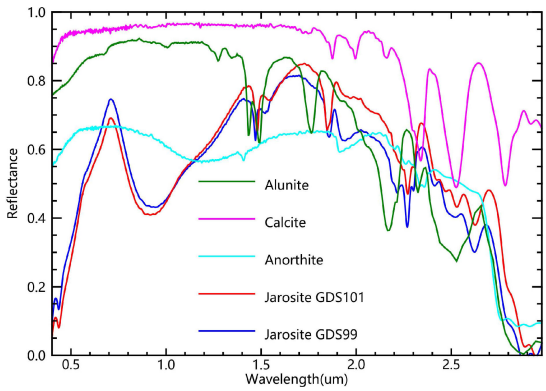

Fig. 4. Spectral characteristic curves of five endmembers.

of our algorithm, the experiment is carried out in the case of Gauss white noise pollution with three different SNR: 20, 30, and 40 dB.

TABLE I
SRE, RMSE (10E-2) AND RUNNING TIME (SECONDS) OF EIGHT ALGORITHMS FOR SYNTHETIC DATASET UNMIXING WITH OPTIMAL PARAMETERS

SNR(dB)	Index	NCLS	SUnSAL	CLSUnSAL	R-CoNMF	NCLS-TV	SUnSAL-TV	CLSUnSAL-TV	ICoNMF-TV
20	SRE	2.181	3.1759	6.1495	8.0598	7.354	10.0614	10.143	**10.1617**
	RMSE	2.80	2.43	1.83	1.73	1.52	1.14	1.06	**0.80**
	t	37.233	29.141	69.376	**10.378**	28.382	325.819	328.714	30.848
	λ	0	0.05	1	-	0	0.0005	0.1	0.1
	λ_{TV}	0	0	0	-	0.05	0.1	0.005	0.001
	μ	0.05	0.05	0.02	0.1	0.1	0.5	0.04	0.1
30	SRE	6.157	7.0552	10.1248	13.7433	13.469	15.0114	15.231	**15.4148**
	RMSE	1.52	1.44	1.35	0.74	0.71	0.67	0.60	**0.45**
	t	23.664	37.547	70.113	**10.287**	103.907	125.999	132.421	28.480
	λ	0	1	1	-	0	0.0005	0.1	0.1
	λ_{TV}	0	0	0	-	0.05	0.1	0.005	0.005
	μ	0.01	0.05	0.02	0.1	1	0.5	0.04	0.1
40	SRE	11.763	12.987	20.047	21.041	22.341	22.878	23.073	**23.098**
	RMSE	0.97	0.92	0.32	0.31	0.29	0.26	0.22	**0.21**
	t	16.861	33.950	37.196	**10.115**	115.0246	136.767	117.514	27.939
	λ	0	0.01	1	-	0	0.0005	0.1	0.1
	λ_{TV}	0	0	0	-	0.05	0.005	0.005	0.005
	μ	0.01	0.05	0.02	0.1	0.05	0.1	0.04	0.1

TABLE II
RMSE (10E-2) OF THREE ALGORITHMS FOR SIMILAR ENDMEMBERS UNMIXING WITH OPTIMAL PARAMETERS

Endmember	SUnSAL-TV	CLSUnSAL-TV	ICoNMF-TV
Jarosite GDS101	0.310	0.278	0.273
Jarosite GDS99	0.279	0.293	0.251

B. Performance Discriminators

The performance discriminators adopted in our experiment to measure the quality of the reconstruction of spectral mixtures are the signal to reconstruction error (SRE) and the root mean square error (RMSE). We use these two measures instead of only the classical RMSE as SRE gives more information regarding the power of the error in relation to the power of the signal. The higher the SRE(dB), the lower the RMSE, the better the unmixing performance. The definitions are as in

$$\text{SRE(dB)} \equiv 10 \lg \frac{E[\|\mathbf{Y}\|_2^2]}{E[\|\mathbf{Y} - \mathbf{AX}\|_2^2]} \tag{27}$$

$$\text{RMSE(dB)} \equiv \sqrt{\frac{1}{p \times n} \sum_{i=1}^{p} \sum_{j=1}^{n} (\mathbf{X}_{ij} - \mathbf{S}_{ij})^2} \tag{28}$$

where $\mathbf{Y}$ is the real image data; $\mathbf{A}$ and $\mathbf{X}$ are the rebuild mixing and abundance data by unmixing algorithms; $\mathbf{S}$ is the real abundance data; p is the number of estimate endmembers; and n is the number of pixels.

C. Results and Analysis

In this section, we test the performance of the proposed TV regularizer combined with CoNMF formulation using the simulated data cubes. In all the tests using the TV regularizer on top of sparse unmixing approaches (NCLS-TV, SUnSAL-TV, and CLSUnSAL-TV), we considered the first-order pixel neighborhood system. We also include the original NCLS, SUnSAL, CLSUnSAL, and R-CoNMF formulations. The test environment for this section is Intel Core i5 CPU 3.20 GHz, RAM 4.0 GB, MATLAB R2016a. The algorithms are tested using different values of the parameters λ and $\lambda_{TV} \in 0.0001, 0.0005, 0.001, 0.005, 0.01, 0.05, 0.1, 0.5, 1, 5$, and $\mu \in 0.01, 0.02, 0.03, 0.04, 0.05, 0.08, 0.1, 0.2, 0.3, 0.4, 0.5, 0.8, 1$. All possible combinations of these parameters are considered shown in Fig. 3. Table I shows the SRE(dB) and RMSE results achieved by the different tested methods with the simulated dataset, using all considered SNR levels. In this table, we only report the best scores obtained across the considered parameter range.

From Table I, we can conclude that the inclusion of the TV regularizer and CoNMF term offer the potential to improve unmixing performance. For high SNR values, the improvements

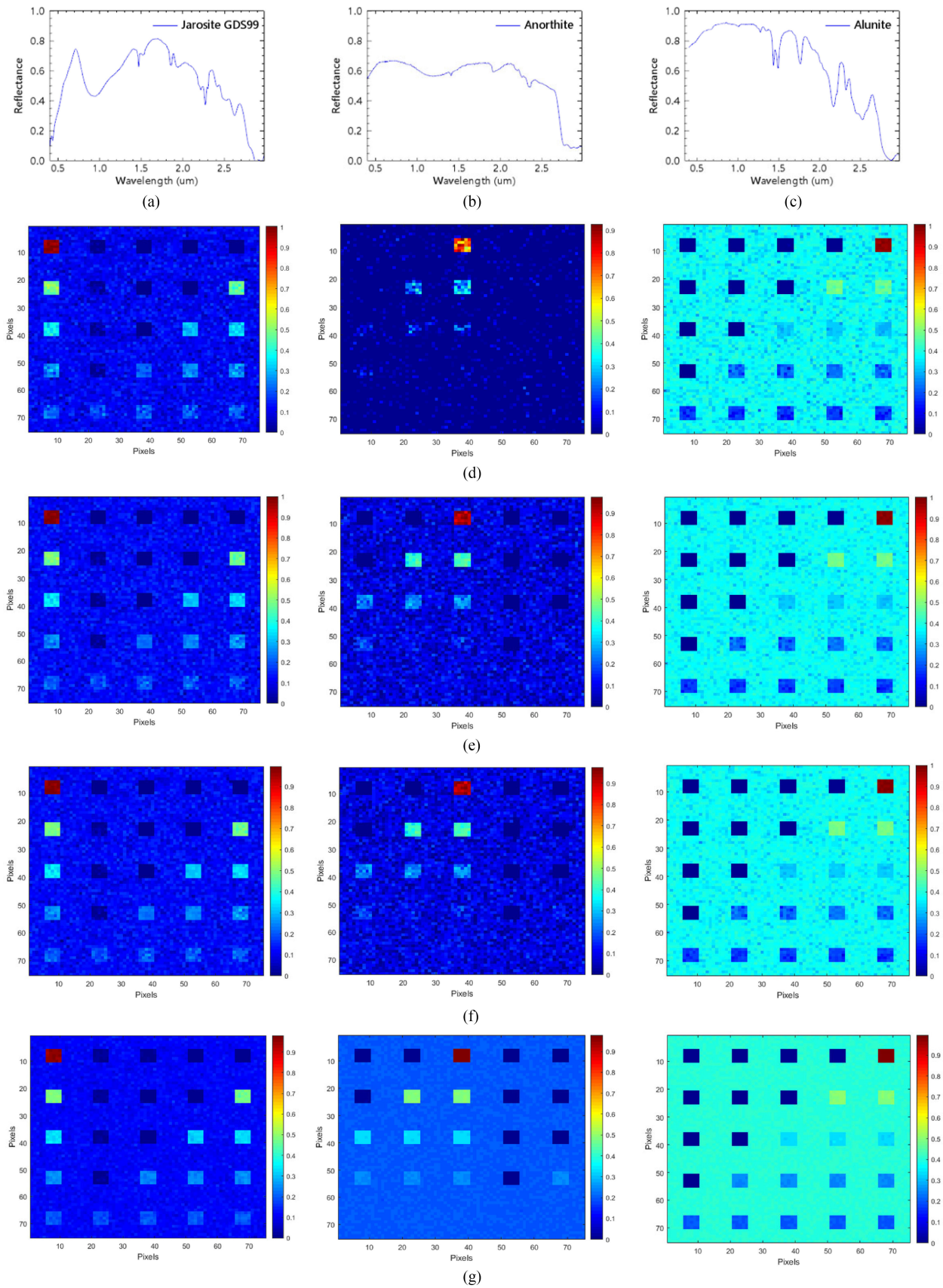
Jarosite GDS99
Anorthite
Alunite
Reflectance
Wavelength (um)
Pixels
(a)
(b)
(c)
(d)
(e)
(f)
(g)

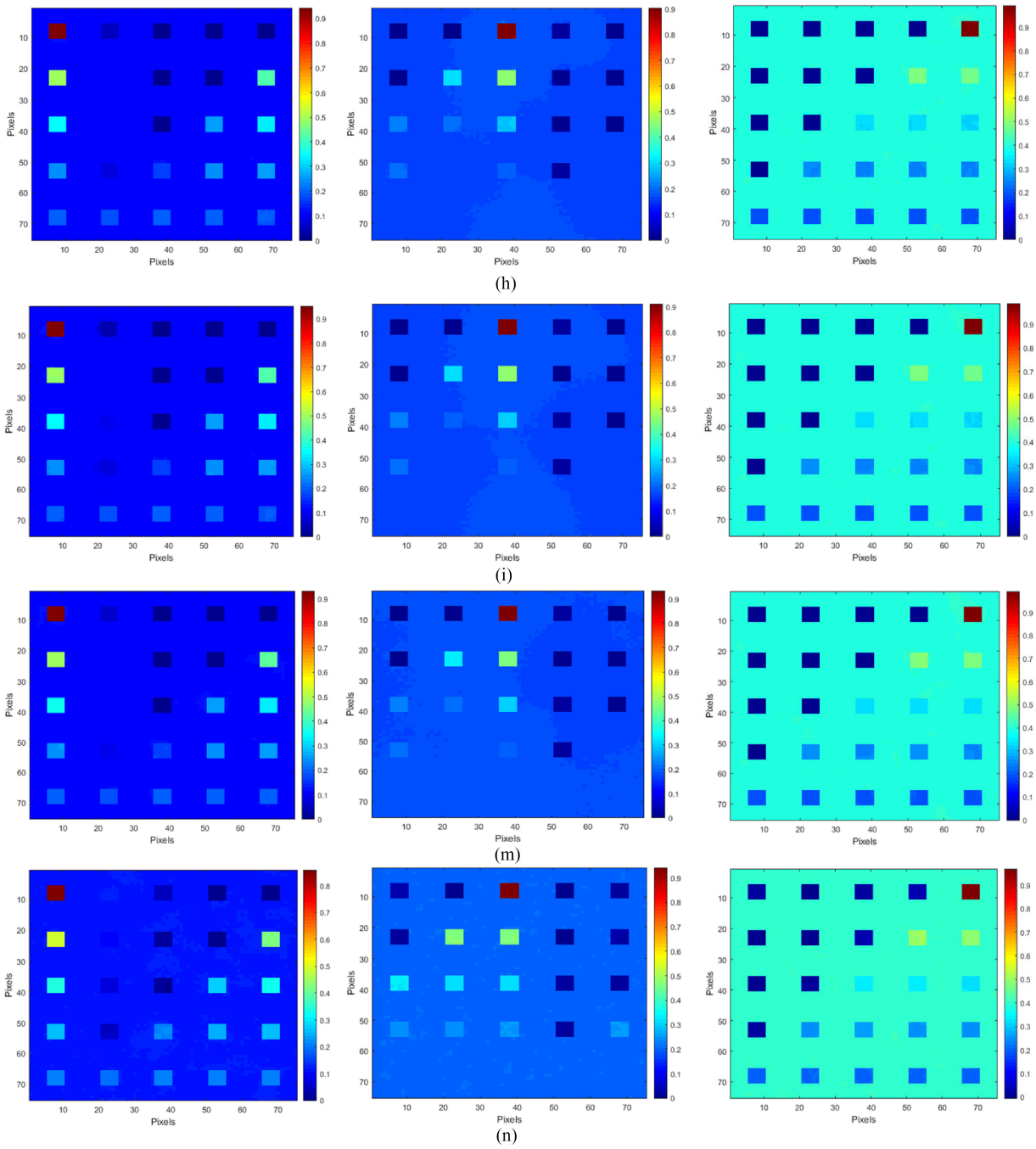

Fig. 5. Extracted abundance maps of eight methods for the simulated dataset when SNR = 40 dB. The parameter settings are reported in Table I. (a) Spectral curve of Endmember 1. (b) Spectral curve of Endmember 2. (c) Spectral curve of Endmember 3. (d) NCLS. (e) SUnSAL. (f) CLSUnSAL. (g) R-CoNMF. (h) NCLS-TV. (i) SUnSAL-TV. (m) CLSUnSAL-TV. (n) ICoNMF-TV.

of TV terms about the standard sparse unmixing formulations (NCLS, SUnSAL, and CLSUnSAL) and R-CoNMF are not significant. This is due to the fact that these methods are able to recover the fractional abundances with good accuracy, with low noise conditions. However, as the noise increases, the TV term becomes more important and improves significantly the quality of unmixing results as it can be observed in the results of NCLS-TV, SUnSAL-TV, and CLSUnSAL-TV for SNR = 20 dB in Table I. Note also that the NCLS-TV, SUnSAL-TV, CLSUnSAL-TV, and ICoNMF-TV provide results which are not very different, which means that the TV regularizer imposes essentially a kind of sparsity in these solutions. As we expected to happen, the TV term is still important dominated by high noise, in which ICoNMF-TV performs clearly better than CLSUnSAL-TV. And for all SNR values, the optimization effect of the non-negative matrix factorization method (CoNMF) compared to three standard sparse formulations (NCLS, SUnSAL, and CLSUnSAL) is distinct. Since the NMF algorithm

itself can process the matrix data as a whole, it is more likely to obtain a relatively superior solution than the standard methods. Although it is expected to happen, the TV term is still important, since ICoNMF-TV performs better than R-CoNMF. R-CoNMF uses the sparse regression methods (SUnSAL and CLSUnSAL) to solve the objective function. In Table I, although it greatly shortens the unmixing time, the accuracy is still lower than some TV regularizers on top of sparse unmixing approaches such as CLSUnSAL-TV. Table II shows the unmixing efficiency of three algorithms for the two similar endmembers with optimal parameters in 40 dB. We can conclude that ICoNMF-TV still has better efficiency than other TV-based methods for similar endmembers. Based on the NMF model, ICoNMF-TV uses these TV regularizers for iteration. We have to admit that ICoNMF-TV takes a little longer time than R-CoNMF. However, the accuracy exceeds all the above algorithms.

For visual purposes, Fig. 5 displays the abundance maps estimated at SNR $= 40$ dB for three randomly selected endmembers in the simulated dataset. Since the abundance maps for other endmembers behaved similarly, we only report the results observed for Endmembers 1, 3, and 5. The abundance maps showed in Fig. 5 were estimated with optimal values for parameters λ and λ_{TV}. The first row are the spectrums of the three endmembers in the spectral library, which are Jarosite GDS99, Anorthite, and Alunite. The other rows, respectively, show the abundance maps estimated by eight methods at SNR $= 40$ dB. From Fig. 5, it can be seen that the TV regularizer improves both the sparse regression methods (NCLS, SUnSAL, and CLSUnSAL) and NMF solution (R-CoNMF), which almost have no noise points. Besides, NMF solutions (R-CoNMF and ICoNMF-TV) exhibit more abundance information of the little squares regions with clearer boundaries than other methods. Qualitatively, we can see that the areas with a high fractional abundance of the selected endmembers are better depicted, while mixed areas with low abundance of the selected endmembers are more homogenized in nature. As reported in Table I, our method achieves both spatial consistency and the materials' spatial distribution with good accuracy.

V. Experiment With Real Dataset

In this section, we test the unmixing performance of ICoNMF-TV ulteriorly in the actual application using real datasets to unmix. The goal is to illustrate visually the influence of the TV regularizer and CoNMF term in the real unmixing results. The section is organized as follows. Section V-A describes how the real dataset is developed. Section V-B concludes the visual interpretation reported in the real unmixing results.

A. Real Dataset

Jasper Ridge is a popular hyperspectral data used in unmixing methods with 512×614 pixels. Each pixel is recorded by 224 channels ranging from 0.38 to 2.5 μm. Considering this hyperspectral image is too complex to get the ground truth, we only use a subimage of 100×100 pixels. After removing the channels $1-3$, $108-112$, $154-166$, and $220-224$ for the dense water vapor and atmospheric effects, we remain 198 channels. Fig. 6 shows the color image of this dataset.

Fig. 6. Jasper Bridge dataset. This dataset is available online[1].

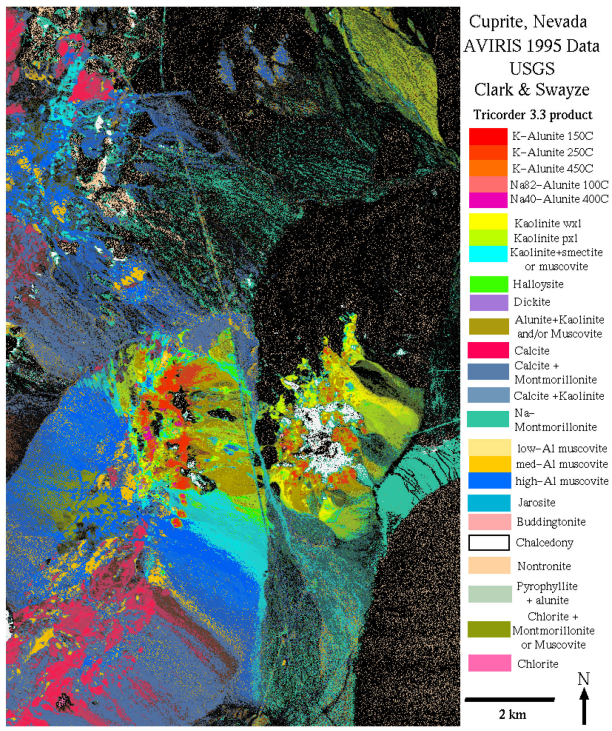

Fig. 7. Cuprite dataset. This dataset is available online[2].

Cuprite Dataset is one of the most well-known hyperspectral datasets used in the HSU study, available online in reflectance units. The portion used to validate the performance of our algorithm corresponds to a 250×190-pixel subset. The dataset consists of 224 spectral bands from 0.4 to 2.5 μm, with a spectral resolution of 10 nm. Due to the water absorption and high noise in some bands, bands $1-2$, $105-115$, $150-170$, and $223-224$ are removed, with 188 bands remained. For illustrative purposes, Fig. 7 displays a mineral map drawn in 1995 by USGS.

B. Results and Analysis

There are four endmembers in the Jasper Bridge dataset and ten endmembers in the Cuprite dataset. We select the number

[1]Online. [Available]: https://goo.gl/images/2edgZU
[2]Online. [Available]: http://speclab.cr.usgs.gov

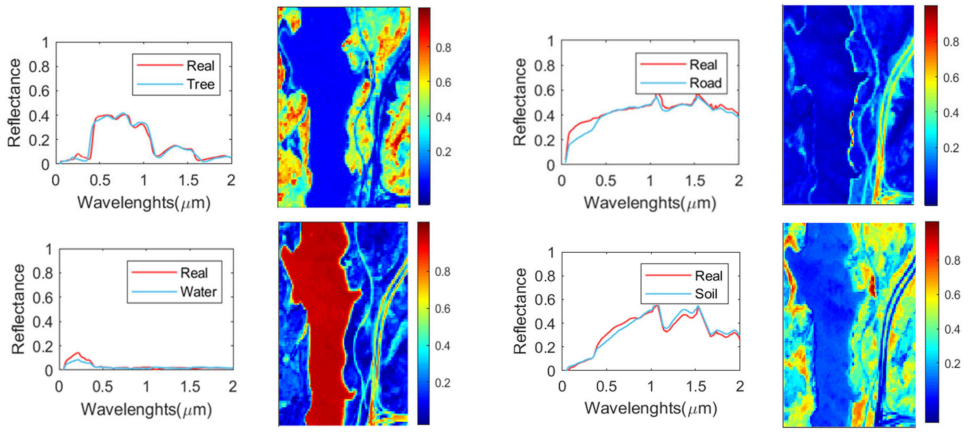

Fig. 8. Reconstracted abundance maps and spectral signature comparisons of ICoNMF-TV method for the Jasper Bridge dataset.

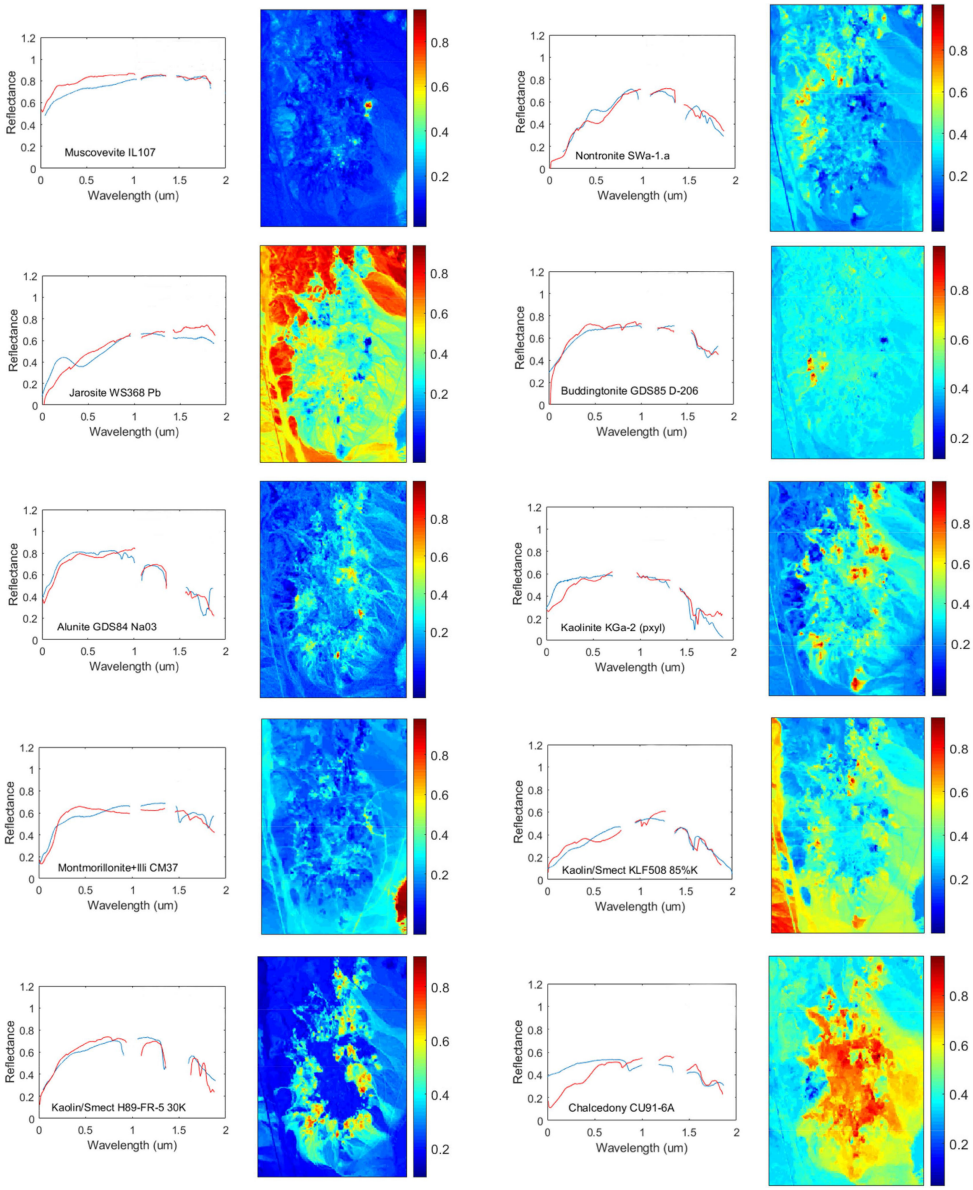

Fig. 9. Reconstracted abundance maps and spectral signature comparisons of ICoNMF-TV method for the Cuprite dataset. The comparison is between groundtruth (blue lines) and ICoNMF-TV (red lines).

TABLE III
SRE, RMSE (10E-2) AND RUNNING TIME (SECONDS) OF EIGHT ALGORITHMS FOR JASPER BRIDGE DATASET UNMIXING

Index	NCLS	SUnSAL	CLSUnSAL	R-CoNMF	NCLS-TV	SUnSAL-TV	CLSUnSAL-TV	ICoNMF-TV
SRE	3.714	5.596	8.314	10.765	8.231	12.012	11.859	**12.212**
RMSE	3.12	2.78	2.19	0.83	1.45	1.08	0.79	**0.43**
t	40.351	35.536	71.413	**9.723**	24.153	305.113	314.208	20.792

TABLE IV
SRE, RMSE (10E-2), AND RUNNING TIME (SECONDS) OF EIGHT ALGORITHMS FOR CUPRITE DATASET UNMIXING

Index	NCLS	SUnSAL	CLSUnSAL	R-CoNMF	NCLS-TV	SUnSAL-TV	CLSUnSAL-TV	ICoNMF-TV
SRE	3.946	4.168	7.235	17.801	6.799	15.541	18.345	**19.225**
RMSE	2.79	2.41	1.33	0.43	1.29	0.64	0.47	**0.35**
t	61.975	63.744	82.003	**56.008**	60.545	398.218	429.551	74.022

of endmembers commonly used in past research. The reported results are the average result of 20 times shown in Table III and Table IV. We analyze the performance of TV regularizer and the CoNMF term to estimate the abundance of fractions and spectral signatures. Figs. 8 and 9 displays, for every endmember extracted by the ICoNMF-TV algorithm, a plot of the estimated endmember and its corresponding USGS library spectral signature and the extracted fractional abundance map. The coincidences between every endmember and its corresponding library spectral signature are established by using visual interpretation of the extracted abundance regarding to the reference map in Figs. 6 and 7. To show the unmixing efficiency for the different number of endmembers, we tested on distinct datasets. This article tested on synthetic datasets $(q = 5)$, Jasper Ridge dataset $(q = 4)$, and Cuprite dataset $(q = 10)$. The results show the proposed method still performs well with the number of endmembers increasing.

For real-world dataset, the corresponding spectral signatures are picked from the spectral library in the software ENVI. The spectral ground truth of Cuprite has not been published. Thus, the selected spectral signatures are generally used to compare with the results as the ground truth. In this process, we notice that the same material has different signatures saved in the library of software ENVI, and there is changeability for even the same kind of material. At this point, we compare extracted endmembers with library signatures in perfect conditions. With above considerations, the results displayed in Figs. 8 and 9 report that the extracted endmembers generally match well with the corresponding library signatures. It is worth noting that the number of endmembers and the mixing degree of these two datasets are quite different. We can conclude that ICoNMF-TV performances stably and efficiently under distinct conditions of real datasets.

VI. CONCLUSION

In this article, a general method named ICoNMF-TV is proposed for hyperspectral image unmixing. First, a TV regularizer is introduced. It not only is an efficient way for improving the accuracy of unmixing in the spatial dimension, but also provides a concise description of the spatial correlation between the image features in the adjacent pixels. Next, based on the NMF method, the CoNMF method is developed to complete batch data processing for the relatively superior solution, with good robustness and accuracy. In the end, the proposed method is evaluated on simulated and real datasets, comparing with the standard sparse formulations (NCLS, SUnSAL, and CLSUnSAL), the sparse-TV formulations (NCLS-TV, SUnSAL-TV, and CLSUnSAL-TV), and the NMF method (R-CoNMF), and shows its effectiveness through intensive comparisons and analyses. However, it should be noticed that this method still runs quite slower than the NMF method, which should be solved by optimizing the calculation process in the future. Since in this issue, we only consider first-order neighborhood systems in the definition, another relevant topic deserving research is the applicability for second-order conditions.

ACKNOWLEDGMENT

The authors would like to thank G. Liu for his feedback on the text.

REFERENCES

[1] N. Keshava and J. Mustard, "Spectral unmixing," *IEEE Signal Process. Mag.*, vol. 19, no. 1, pp. 44–57, Jan. 2002.
[2] Q. Wang, M. Chen, F. Nie, and X. Li, "Detecting coherent groups in crowd scenes by multiview clustering," *IEEE Trans. Pattern Anal. Mach. Intell.*, vol. 42, no. 1, pp. 46–58, Jan. 2020.
[3] Q. Wang, J. Lin, and Y. Yuan, "Salient band selection for hyperspectral image classification via manifold ranking," *IEEE Trans. Neural Netw. Learn. Syst.*, vol. 27, no. 6, pp. 1279–1289, Jun. 2016.
[4] J. Nascimento and J. Bioucas-Dias, "Hyperspectral subspace identification," *IEEE Trans. Geosci. Remote Sens.*, vol. 46, no. 8, pp. 2435–2445, Aug. 2008.
[5] X. Xu, J. Li, C. Wu, and A. Plaza, "Regional clustering-based spatial preprocessing for hyperspectral unmixing," *Remote Sens. Environ.*, vol. 204, no. 3, pp. 333–346, 2018.
[6] D. Lee and H. Seung, "Learning the parts of objects by non-negative matrix factorization," *Nature*, vol. 401, no. 6755, pp. 788–791, 1999.
[7] M. Iordache and J. Bioucas-Dias, "Total variation spatial regularization for sparse hyperspectral unmixing," *IEEE Trans. Geosci. Remote Sens.*, vol. 50, no. 11, pp. 4484–4502, Nov. 2012.

[8] C. Yunjie, W. Gedong, and S. Le, "A novel linear hyperspectral unmixing method based on collaborative sparsity and total variation," *Acta Automatica Sinica*, vol. 44, no. 1, pp. 116–128, 2018.
[9] J. Li and J. Bioucas-Dias, "Robust collaborative nonnegative matrix factorization for hyperspectral unmixing," *IEEE Trans. Geosci. Remote Sens.*, vol. 54, no. 10, pp. 6076–6090, Oct. 2016.
[10] J. M. Bioucas-Dias, "A variable splitting augmented lagrangian approach to linear spectral unmixing," in *Proc. IEEE 1st Workshop Hyperspectral Image Signal Process.: Evol. Remote Sens.*, 2009, pp. 1–4.
[11] M. Iordache and J. Bioucas-Dias, "Collaborative sparse regression for hyperspectral unmixing," *IEEE Trans. Geosci. Remote Sens.*, vol. 52, no. 1, pp. 341–354, Jan. 2014.
[12] J. Bioucas-Dias, A. Plaza, and N. Dobigeon, "Hyperspectral unmixing overview: Geometrical, statistical, and sparse regression-based approaches," *IEEE J. Sel. Topics Appl. Earth Observ. Remote Sens.*, vol. 5, no. 2, pp. 354–379, Apr. 2012.
[13] H. Wei, H. Yangyu, L. Wei, Z. Fan, and L. Hengchao, "Endmember extraction from highly mixed data using minimum volume constrained non-negative matrix factorization," *IEEE Trans. Geosci. Remote Sens.*, vol. 45, no. 3, pp. 765–777, Mar. 2007.
[14] S. Zhang and A. Agathos, "Robust minimum volume simplex analysis for hyperspectral unmixing," *IEEE Trans. Geosci. Remote Sens.*, vol. 55, no. 11, pp. 6431–6439, Nov. 2017.
[15] J. Nascimento and J. Dias, "Vertex component analysis: A fast algorithm to unmix hyperspectral data," *IEEE Trans. Geosci. Remote Sens.*, vol. 43, no. 4, pp. 898–910, Apr. 2005.
[16] J. Li, A. Agathos, and D. Zaharie, "Minimum volume simplex analysis: A fast algorithm for linear hyperspectral unmixing," *IEEE Trans. Geosci. Remote Sens.*, vol. 53, no. 19, pp. 5067–5082, Sep. 2015.
[17] O. Eches, N. Dobigeon, and C. Mailhes, "Bayesian estimation of linear mixtures using the normal compositional model application to hyperspectral imagery," *IEEE Trans. Image Process.*, vol. 19, no. 6, pp. 1403–1413, Jun. 2010.
[18] N. Dobigeon, S. Moussaoui, and M. Coulon, "Joint Bayesian endmember extraction and linear unmixing for hyperspectral imagery," *IEEE Trans. Signal Process.*, vol. 57, no. 11, pp. 4355–4368, Nov. 2009.
[19] R. Wang, H.-C. Li, A. Pizurica, J. Li, A. Plaza, and W. J. Emery, "Hyperspectral unmixing using double reweighted sparse regression and total variation," *IEEE Geosci. Remote Sens. Lett.*, vol. 14, no. 7, pp. 1146–1150, Jul. 2017.
[20] J. Li, J. M. Bioucas-Dias, and A. Plaza, "Collaborative nonnegative matrix factorization for remotely sensed hyperspectral unmixing," in *Proc. IEEE Int. Geosci. Remote Sens. Symp.*, 2012, pp. 3078–3081.
[21] P. Hoyer, "Non-negative sparse coding," in *Proc. 12th IEEE Workshop Neural Netw. Signal Process.*, 2002, pp. 557–565.
[22] Y. Qian, S. Jia, J. Zhou, and A. Robles-Kelly, "Hyperspectral unmixing via $l\_\{1/2\}$ sparsity-constrained nonnegative matrix factorization," *IEEE Trans. Geosci. Remote Sens.*, vol. 49, no. 11, pp. 4282–4297, Nov. 2011.
[23] X.-R. Feng, H.-C. Li, J. Li, Q. Du, A. Plaza, and W. J. Emery, "Hyperspectral unmixing using sparsity-constrained deep nonnegative matrix factorization with total variation," *IEEE Trans. Geosci. Remote Sens.*, vol. 56, no. 10, pp. 6245–6257, Oct. 2018.
[24] M. Iordache and J. Bioucas-Dias, "Sparse unmixing of hyperspectral data," *IEEE Trans. Geosci. Remote Sens.*, vol. 49, no. 6, pp. 2014–2039, Jun. 2011.
[25] R. Wang, H.-C. Li, W. Liao, X. Huang, and W. Philips, "Centralized collaborative sparse unmixing for hyperspectral images," *IEEE J. Sel. Topics Appl. Earth Observ. Remote Sens.*, vol. 10, no. 5, pp. 1949–1962, May 2017.
[26] Y. Altmann, M. Pereyra, and J. Bioucas-Dias, "Collaborative sparse regression using spatially correlated supports application to hyperspectral unmixing," *IEEE Trans. Image Process.*, vol. 24, no. 12, pp. 5800–5811, Dec. 2015.
[27] M. Iordache, J. Bioucas-Dias, and A. Plaza, "Hyperspectral unmixing via multiple signal classification and collaborative sparse regression," *IEEE Trans. Geosci. Remote Sens.*, vol. 52, no. 7, pp. 4364–4382, Jul. 2014.
[28] Q. Wang, J. Wan, F. Nie, B. Liu, C. Yan, and X. Li, "Hierarchical feature selection for random projection," *IEEE Trans. Neural Netw. Learn. Syst.*, vol. 30, no. 5, pp. 1581–1586, May 2019.
[29] J. Li, X. Li, and B. Huang, "Hopfield neural network approach for supervised nonlinear spectral unmixing," *IEEE Geosci. Remote Sens. Lett.*, vol. 13, no. 7, pp. 1002–1006, Jul. 2016.
[30] G. Licciardi and F. Frate, "Pixel unmixing in hyperspectral data by means of neural networks," *IEEE Trans. Geosci. Remote Sens.*, vol. 49, no. 11, pp. 4163–4172, Nov. 2011.
[31] X. Fu, K. Ma, and H. Chan, "Self-dictionary sparse regression for hyperspectral unmixing: Greedy pursuit and pure pixel search are related," *IEEE J. Sel. Topics Signal Process.*, vol. 9, no. 6, pp. 1128–1141, Sep. 2015.
[32] L. Qiang, W. Xv, and C. Lei, "Hyperspectral unmixing algorithm based on neural network and differential search," *J. Optoelectron. Laser*, vol. 27, no. 12, pp. 1357–1364, 2016.
[33] G. Trigeorgis, K. Bousmalis, S. Zafeiriou, and B. Schuller, "A deep semi-nmf model for learning hidden representations," in *Proc. Int. Conf. Mach. Learn.*, 2014, pp. 1692–1700.
[34] K. Huang, N. D. Sidiropoulos, and A. Swami, "Non-negative matrix factorization revisited: Uniqueness and algorithm for symmetric decomposition," *IEEE Trans. Signal Process.*, vol. 62, no. 1, pp. 211–224, Jan. 2014.
[35] Z. Yang, Y. Xiang, K. Xie, and Y. Lai, "Adaptive method for nonsmooth nonnegative matrix factorization," *IEEE Trans. Neural Netw. Learn. Syst.*, vol. 28, no. 4, pp. 948–960, Apr. 2017.
[36] H. Fang, A. Li, T. Wang, and H. Xu, "Hyperspectral unmixing using double-constrained multilayer NMF," *Remote Sens. Lett.*, vol. 10, no. 3, pp. 224–233, 2019.
[37] H. Attouch, J. Bolte, P. Redont, and A. Soubeyran, "Proximal alternating minimization and projection methods for nonconvex problems: An approach based on the Kurdyka-Łojasiewicz inequality," *Math. Oper. Res.*, vol. 35, no. 2, pp. 438–457, 2010.
[38] L. Grippof and M. Sciandrone, "Globally convergent block-coordinate techniques for unconstrained optimization," *Optim. Methods Softw.*, vol. 10, no. 4, pp. 587–637, 1999.

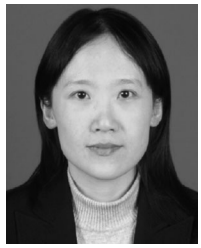

Yuan Yuan (Senior Member, IEEE) is currently a Professor with the School of Computer Science and with the Center for OPTical IMagery Analysis and Learning, Northwestern Polytechnical University, Xi'an, China. She has authored or coauthored more than 150 papers, including about 100 in reputable journals, such as the *IEEE Transactions and Pattern Recognition*, and also conference papers in CVPR, BMVC, ICIP, and ICASSP. Her current research interests include visual information processing and image/video content analysis.

Zihan Zhang received the B.E. degree in information security from the Northwestern Polytechnical University, Xi'an, China, in 2018. She is currently working toward the M.S. degree in computer science with the Center for OPTical IMagery Analysis and Learning, School of Computer Science, Northwestern Polytechnical University, Xi'an, China.

Her research interests include hyperspectral image unmixing and computer vision.

Qi Wang (Senior Member, IEEE) received the B.E. degree in automation and the Ph.D. degree in pattern recognition and intelligent systems from the University of Science and Technology of China, Hefei, China, in 2005 and 2010, respectively.

He is currently a Professor with the School of Computer Science and with the Center for OPTical IMagery Analysis and Learning, Northwestern Polytechnical University, Xi'an, China. His research interests include computer vision and pattern recognition.